

1

2

3

4

5

Tunable Protein Crystal Size Distribution via Continuous

6

Slug-Flow Crystallization with Spatially Varying Temperature

7

8

Nicholas J. Mozdierz¹, Moo Sun Hong¹, Yongkyu Lee^{1,2}, Moritz H. P. Benisch^{1,3}, Mo Jiang⁴,

9

Allan S. Myerson¹, and Richard D. Braatz^{1†}

10

11

12

13

14

¹*Dept. of Chemical Engineering, Massachusetts Institute of Technology, Cambridge, MA, USA*

15

²*Dept. of Chemical & Biological Engineering, Seoul National University, Seoul, South Korea*

16

³*Institute for Chemical & Bioengineering, ETH Zurich, Zurich, Switzerland*

17

⁴*Dept. of Chemical & Life Science Engineering, Virginia Commonwealth University, Richmond, VA, USA*

18

19

20

† braatz@mit.edu

21

Abstract

22 Accompanied with the growth of the biopharmaceuticals market has been an interest in
23 developing processes with increased control of product quality attributes at low manufacturing
24 cost, with one of the approaches being through genuinely continuous manufacturing processes.
25 Part of this interest is in new drug product formulations that extend shelf-life and improve the
26 patient experience. Some of these drug product formulations require the production of protein
27 crystals of controlled size distribution. This article describes a continuous tubular crystallizer in
28 which the size distribution of the produced protein crystals is tuned by controlling the spatial
29 temperature along the tube. Under the proper buffer and pH condition, the magnitude and
30 dispersion of product protein crystals are reproducibly manipulated using a fully controlled
31 temperature profile over a 25- to 30-minute residence time, and the formation of amorphous
32 precipitates can be achieved under higher supersaturation condition via the addition of
33 concentrated precipitant for drug products in which higher solubility is desired. The tunable
34 continuous process for protein crystallization has the potential to become a low-cost platform
35 technology for producing protein crystals for a variety of biologic drug product formulations.

Keywords

37 Continuous manufacturing; pharmaceutical crystallization; continuous crystallization;
38 population balance modeling; tubular crystallization; slug-flow crystallization

39 **1 . Introduction**

40 From an industrial perspective, an opportunity exists to develop scalable non-chromatographic
41 protein separations methods that disrupt the traditional batch-wise paradigm and support
42 continuous purification modes¹⁻³. Despite efforts to demonstrate the future viability of sequential
43 ‘bind-and-elute’ chromatography, resin-based adsorption processes are costly and widely
44 perceived within the biomanufacturing field to be a major process bottleneck^{1,4-6}. Technologies
45 such as periodic counter-current chromatography (PCC), simulated moving bed chromatography
46 (SMB), and multi-column counter-current solvent gradient purification (MCSGP) have been
47 demonstrated to reduce this bottleneck⁷. Each of these processes, however, employs more
48 columns, valves, and pumps than sequential chromatography, substantially increasing both system
49 complexity and capital equipment costs^{2,8,9}. Further, given that they require the same number of
50 stages as sequential chromatography to achieve the same purification efficiency – but operate at
51 higher throughputs using more resin – PCC, SMB, and MCSGP have operating expenses (OPEX)
52 costs that scale linearly with respect to conventional techniques. In contrast, non-chromatographic
53 protein purification methods such as precipitation, aqueous two-phase extraction (ATPE), and
54 crystallization are relatively simple to execute, require a small initial capital investment, and boast
55 OPEX costs (primarily buffers/solvents) that scale sub-linearly with throughput^{2,6,7}. A single
56 example of the application of each of these three techniques to continuous protein purification has
57 been published¹⁰⁻¹². In addition to reducing facility footprints, precipitation, ATPE, and
58 crystallization have the potential to dramatically increase equipment utilization, allowing the
59 biopharmaceutical sector to realize higher productivities and improved operational flexibility^{2,3,7}.
60 These methods could also support the robust control of short product residence times, allowing for

61 the rapid recovery of labile protein and standardization of critical quality attributes across each
62 lot^{3,7}. Finally, the improved purification efficiency gleaned by coupling these techniques with
63 ‘clean’ expression hosts (*e.g.*, *Komagataella phaffii*), as well as their amenability to scale-out by
64 parallelization^{13,14}.

65 Despite its potential cost-effectiveness and scalability, however, the intrinsic difficulty of
66 optimizing and controlling protein crystallization has prevented its broad adoption as a preparative
67 purification technique^{7,15}. Specifically, a generalized set of heuristics governing the myriad
68 physical, chemical, and biochemical factors that can impact protein crystal nucleation and growth
69 has yet to be realized¹⁵⁻¹⁷. Consequently, while a wide range of proteins has been crystallized at
70 the μL scale for structure determination using various combinatorial screening approaches (*e.g.*,
71 hanging and sitting drop vapor diffusion, free interface diffusion, and dialysis), recombinant
72 insulins are the only biopharmaceutical reported to be purified by crystallization at the industrial
73 scale^{7,18}. Studies surrounding the batch crystallization of enzymes (*e.g.* hen egg white lysozyme
74 (HEWL), lipase) and monoclonal antibody fragments from both homo- and heterogeneous
75 mixtures at volumes ranging from 100 mL to 1 L represent promising demonstrations of this
76 technique as a method for ‘at-scale’ purification, but fall short of proving industrial applicability¹⁵.

77 In addition, protein crystallization from nearly pure solution is suitable for producing crystals
78 in drug product formulation/delivery¹⁹. Amorphous lyophilizates and aqueous solutions are
79 commonly used for formulation/delivery but have low stability and high viscosity at high
80 concentration. Crystals have a higher stability and could lead to a better patient experience with
81 consistent controlled properties. For injection, which is currently the primary mode of
82 administration, high viscosity requires a large-bore needle and a high amount of force to push the

83 needle into the body, which is painful for the patient. Experimental results for monoclonal
84 antibodies have demonstrated that injection of a crystalline suspension reduces the syringe force
85 by about 50% for the same protein concentration compared to liquid formulation¹⁵. The injection
86 of crystals also enables the protein to be taken into the blood stream at a slower rate for a more
87 sustained release. In all of these protein crystal-based drug product formulations, the rate of uptake
88 of the biotherapeutic protein molecules into the bloodstream depends critically on the size
89 distribution of the protein crystals.

90 A recent set of experiments has demonstrated tubular designs as viable technologies for protein
91 crystallization^{12,20}. Using a low-cost setup designed around disposable plastic components and
92 syringe pumps, crystallization of HEWL was reported from a purified solution at a rate of 0.72
93 g/h. Such studies have not demonstrated robust feedback process control. In this article, we
94 leverage optimization/control theory – building off from prior art surrounding the tubular
95 crystallization of small molecules and active pharmaceutical ingredients – and develop a flexible
96 flow-through system for the continuous crystallization of therapeutically relevant proteins under
97 feedback control.

98 Here, a fully automated system designed to operate under segmented slug-flow and capable of
99 on-line control of the cooling process is applied to the continuous crystallization of the model
100 protein HEWL. In addition to temperature, pH and buffered precipitant solution are used to control
101 the supersaturation of HEWL at various defined points along the length of the crystallizer. These
102 parameters are carefully combined to permit tuning the particle size distribution (PSD) generated
103 by the counter current heat exchanger (CCHEx) platform under controlled and seeded inlet
104 conditions. The system is further demonstrated that this control is possible over a residence time

105 as short as 25–30 minutes (2x–4x shorter than similar recent reports). Powder X-Ray Diffraction
106 (PXRD) and cross-polarized transmitted light microscopy are used to qualitatively score the
107 relative ratio of amorphous-to-crystalline HEWL generated under each set of conditions tested.
108 The images acquired using cross-polarized light is analyzed using the custom crystal image
109 analysis algorithm designed for adjusting contrast and segmenting overlaid crystal image.

110

111 **2. Experimental method**

112 **2.1. Materials**

113 Hen egg white lysozyme (HEWL) was used as the model protein for all experiments as
114 described. Buffer preparation involved sodium acetate (NaOAc), hydrochloric acid (HCl), HPLC-
115 grade distilled deionized water, and disposable 0.2 μm vacuum filtration systems. A 1 M solution
116 of sodium hydroxide (NaOH) was used to flush the CCHEx crystallizer at the beginning and end
117 of each day of experiments.

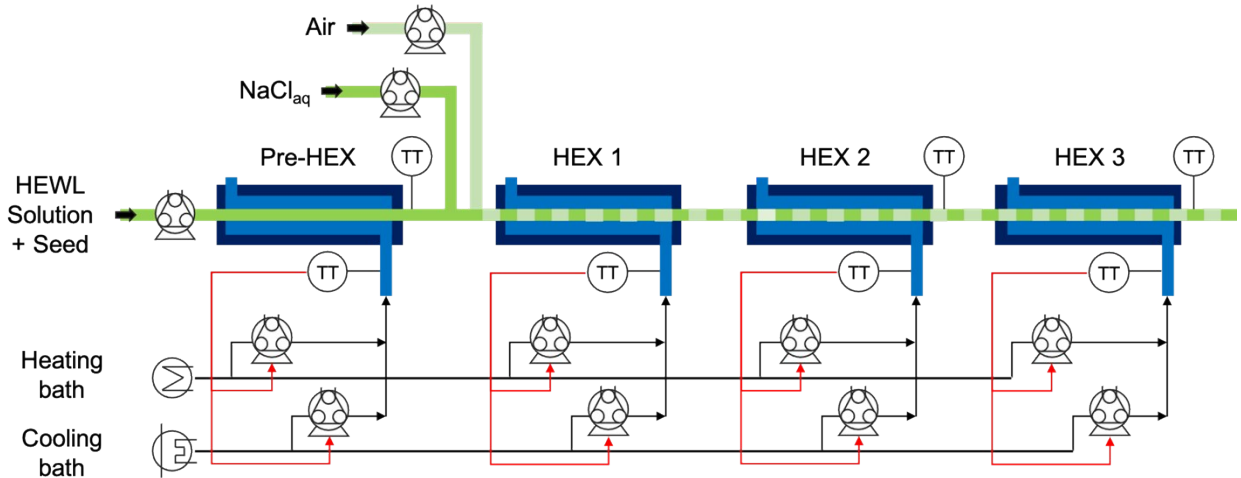
118 Seed solutions for all experiments were prepared by first suspending HEWL in a refrigerated
119 solution of 2% w/v sodium chloride (NaCl) and 100 mM NaOAc (pH 4.0) to a concentration of
120 70 g/L. The suspension was then placed in a water bath held at 30°C and stirred for 3.5 hours.
121 The resulting hazy solution was subsequently vacuum filtered, placed back in the water bath, and
122 allowed to cool spontaneously overnight. Before first use, the seed solution was heated to the
123 appropriate temperature as indicated in Table 1.

124 **2.2. Experimental apparatus**

125 The experimental apparatus in Fig. 1 consists of peristaltic pumps, heat exchangers (HEX),
126 heating and cooling baths, and controlled-temperature water baths^{21,22}. All but one of the
127 components are integrated in a computer used for collecting data and performing real-time control
128 calculations. The precipitant pump containing NaCl aqueous solution was not integrated into the
129 larger control system, as the in-line precipitant mixing was manually set at the beginning of the
130 experiment and was not changed during each experiment. The precipitant solution was stored in a
131 magnetically stirred, jacketed, 1 L, glass, two-necked round-bottom flask plumbed in series with
132 the cold coolant reservoir and seed/feedstock solution Allihn condenser.

133 The temperature-controlled HEWL solution enters the crystallizer from the round-bottom flask
134 at the left in Fig. 1 and traverses a short segment of insulated tubing before transiting through the
135 preliminary heat exchanger (pre-HEX) and mixing with a slipstream of concentrated, chilled, and
136 buffered NaCl. The mixture of HEWL and precipitant then traverse under an indirect
137 ultrasonication probe and mixes with filtered air to form stable liquid slugs. Slug flow is
138 hydrodynamically stable for a very large range of gas and liquid flow rates for the tubing diameter
139 and fluid properties in the experiments in this study, as observed experimentally in consistency
140 with theoretical expressions as detailed in a recent book chapter²³. The slugs then move through
141 HEXs 1, 2, and 3 prior to be collected for imaging and PXRD analysis at the outlet. For all
142 experiments that did not employ concentrated precipitant addition, the air and liquid flow rates
143 into the slugging tee were both 7 mL/min. The air and liquid flow rates into the slugging tee during
144 experiments that involved concentrated precipitant addition were 7 and 9.61 mL/min (HEWL
145 solution 7 mL/min and precipitant solution 2.61 mL/min), respectively. For each HEX, the shell-

146 side flowrate from the peristaltic pumps is given by the proportional-integral (PI) controllers to
147 achieve the set point temperature.



148

149 Figure 1. A process flow diagram of the continuous crystallizer with in-line precipitant mixing capabilities,
150 where HEWL is hen egg white lysozyme, HEX refers to a heat exchanger, and TT refers to a temperature
151 transmitter.

152 2.3. Design of experiments

153 Each of the four sets of experimental conditions tested was designed to expose HEWL
154 transiting the continuous system to markedly different supersaturation conditions while holding
155 constant the residence time of the slugs (Table 1). All temperature and the concentration of
156 precipitant set points were determined with the aid of empirical models fitted to solubility data²⁴.
157 Specifically, Experiment 1 was designed to ‘crash cool’ the HEWL solution immediately upon
158 entering the pre-HEX module by exposure to a maximum instantaneous supersaturation (σ_{max} ,
159 where $\sigma = C/C_{sat} - 1$, C is the HEWL concentration, and C_{sat} is the solubility) equal to ~ 18 .
160 Experiment 2 is designed to reduce σ_{max} to ~ 6.4 and promote dissolution in HEX 1 following
161 primary nucleation in the pre-HEX. Experiment 3 was designed to expose slugs of dissolved and
162 crystalline HEWL to a shallow temperature – and by extension, supersaturation – gradient with

163 σ_{max} of ~ 4.3 in an effort to favor the growth of seed crystals relative to the nucleation of new
 164 particles. Finally, Experiment 4 represents a situation in which σ_{max} was varied aggressively
 165 (~ 220) by using a combination of concentrated precipitant (*i.e.*, NaCl) addition and crash cooling.
 166 Each of Experiments 1–3 was performed in duplicate. This study explores a wide range of
 167 supersaturations to demonstrate the ability of the system to access a very large experimental design
 168 space, and to assess the effects on the product crystals. Further, relative to Experiments 1–3,
 169 Experiment 4 was designed to exploit the generalized phase behavior of protein solutions, which
 170 predicts that extreme values of σ_{max} will preferentially induce the formation of amorphous
 171 precipitates over well-ordered crystals²⁵. In this way, disordered aggregates of HEWL are
 172 generated intentionally as a control to aid in distinguishing crystalline from non-crystalline
 173 samples by both cross-polarized microscopy and PXRD.

174 Table 1. HEWL experimental parameters and set points. T = temperature. Rep. = replicate. Precipitant was
 175 15% w/v NaCl, 57.7 mM NaOAc, pH 4.0 buffer held at 3.0°C.

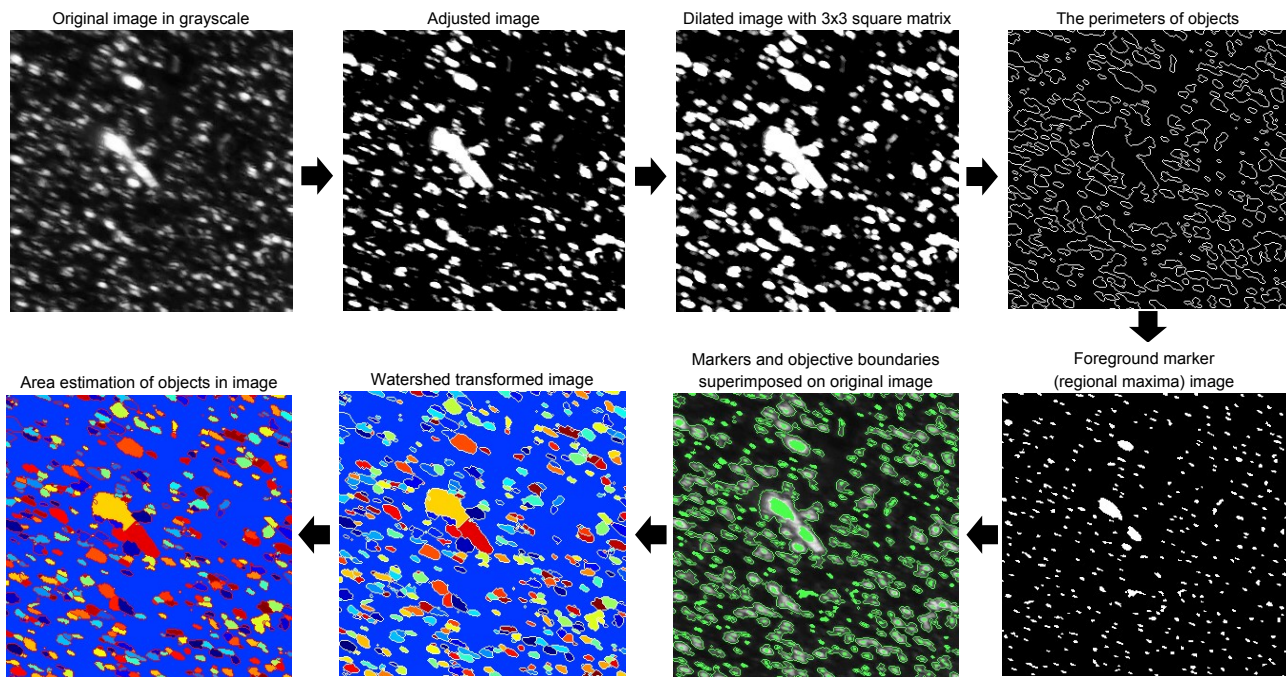
Exp.	Rep.	Seed Bath Temperature (°C)	Temperatures (°C)			
			Pre-HEX	HEX 1	HEX 2	HEX 3
1	1	32.6	5	5	5	23
1	2	32.35	5	5	5	23
2	1	28.65	14	20	11	7
2	2	28.45	14	20	11	7
3	1	23.8	17	15	11	8
3	2	23.9	17	15	11	8
4	1	42	5	5	5	5

176

177 2.4. Automated imaging analysis for particle size distribution

178 For each experiment, a single pulse of HEWL (Table 1) was fed into the continuous
 179 crystallizer. Pulses of air (each 10 s long) bracketed the HEWL to aid in identifying crystal-
 180 containing slugs at the outlet. All slugs of HEWL were collected as they exited the crystallizer in
 181 a single sterile 50 mL conical tube. Four 45 μL droplets of the collected slurry were immediately

182 transferred to an air-dusted microscope slide and protected from evaporation with cover glasses.
183 A set of position matched images of each droplet was then acquired using a microscope fitted with
184 a digital camera, a 10X trinocular eyetube, and 4X/0.10 HI PLAN objective. The resolution of this
185 optical setup was $1\ \mu\text{m}/\text{pixel}$. Light intensity, aperture, and condenser settings were kept constant
186 across all images and all experiments.



187

188 Figure 2. Graphical summary of the image processing algorithm which is a modified version of marker-
189 controlled watershed segmentation for sorting out overlaid crystals.

190 Each of the four cross-polarized micrographs corresponding to a given experiment was
191 analyzed using the watershed algorithm with markers and boundaries described in Fig. 2. First of
192 all, the original color image is mapped to grayscale for adjusting the contrast. The adjusted image
193 is dilated with structuring element neighborhood where pixels are connected along the horizontal
194 or vertical direction for protecting tiny size crystals from eroding process. The boundaries of
195 segmented objects are calculated in pixels and separate the threshold of regions for the watershed

196 method. The foreground markers in the object are obtained by a closing followed by erosion and
197 are superimposed on grayscale image with the boundaries of regions. The magnitudes of markers
198 are modified to regional minima of the objective region and scaled to different integer values. The
199 flooding process is performed from the marker (the regional minima), and the borderline is
200 constructed between the extended regions of different labeled markers. Finally, the area and length
201 of crystals are estimated and used to acquire the particle size distribution.

202 **2.5. Powder x-ray diffraction**

203 Approximately 10 minutes after collection (the time required to perform all imaging described
204 in section 2.3), the remaining slurry from a given experiment was divided into 12 to 15 1.0-mL
205 aliquots and centrifuged at 10,000 g and 22°C for 2 minutes. The resulting supernatant was
206 subsequently aspirated off and discarded. A second identical centrifugation step was employed in
207 the case when bulk liquid remained after aspiration. Pellets were then stored under ambient
208 conditions for ~4 hours prior to analysis by PXRD. The obtained crystals were crushed using a
209 mortar and pestle in order to maximize the number of visible crystal faces²⁶.

210 PXRD was performed using a PANalytical X'Pert PRO diffractometer. The instrument was
211 configured as described in a past study²⁶ and operated at a tension of 45 kV and an anode current
212 of 40 mA. All scans were conducted under the following programmable settings to maximize
213 resolution at low angles: 3.507°–13.5° 2θ range; 0.0167113° step; 455.295 s step time; 0.004661°/s
214 scan speed; and 1 rps spinner stage rotation speed. Each scan analyzed the equivalent of at least 8
215 pellets pressed onto a zero-background sample tray. A blank sample tray diffractogram was
216 acquired under these same settings.

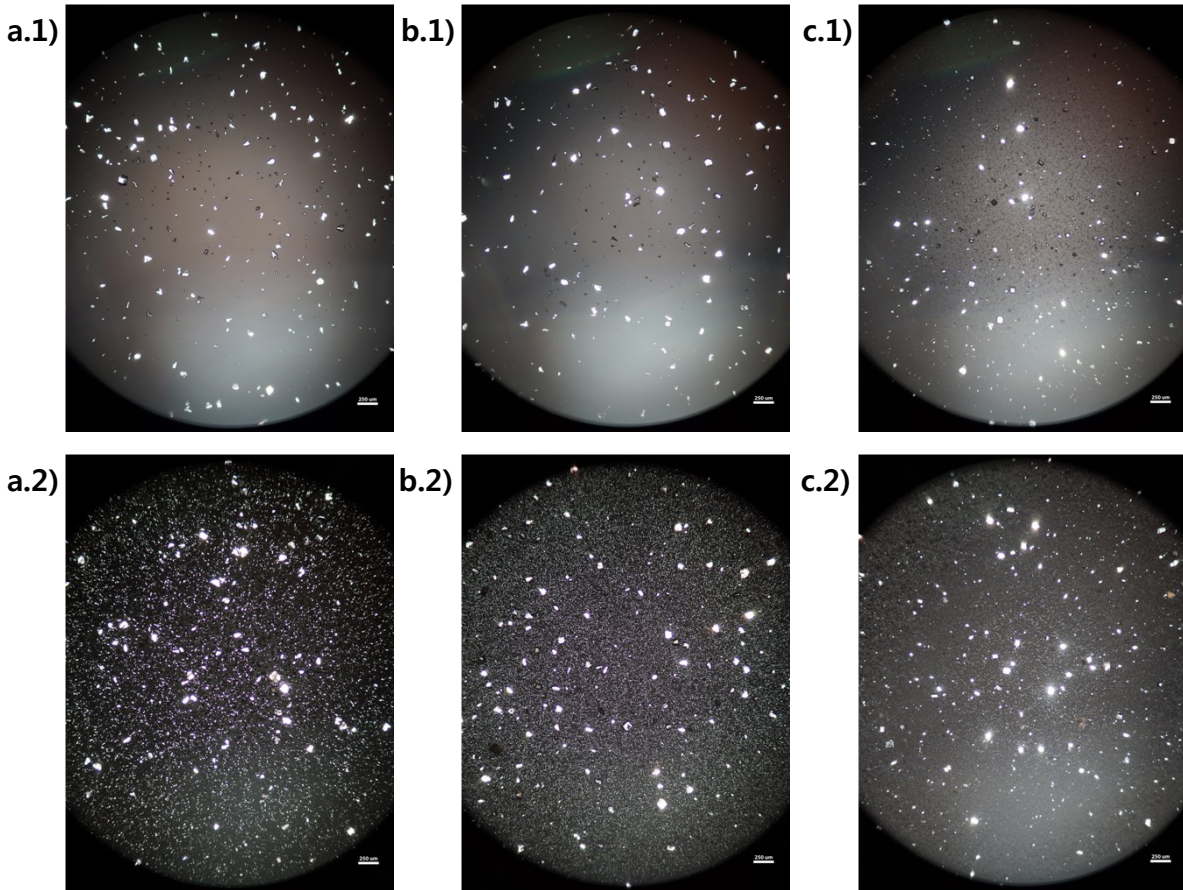
217 A negative control diffractogram of the 2% w/v NaCl and 100 mM NaOAc (pH 4.0) buffer
218 used to prepare all HEWL solutions were obtained using the same instrument and hardware
219 configuration noted above. 75 mL of the buffer was first boiled on a hot plate under stirring for 2
220 hours to evaporate most of the bulk liquid. The remaining slurry was then dried in a vacuum oven
221 overnight to yield a powder of crystalline NaCl and NaOAc in a mass ratio identical to that in the
222 original buffer.

223

224 **3. Results and Discussion**

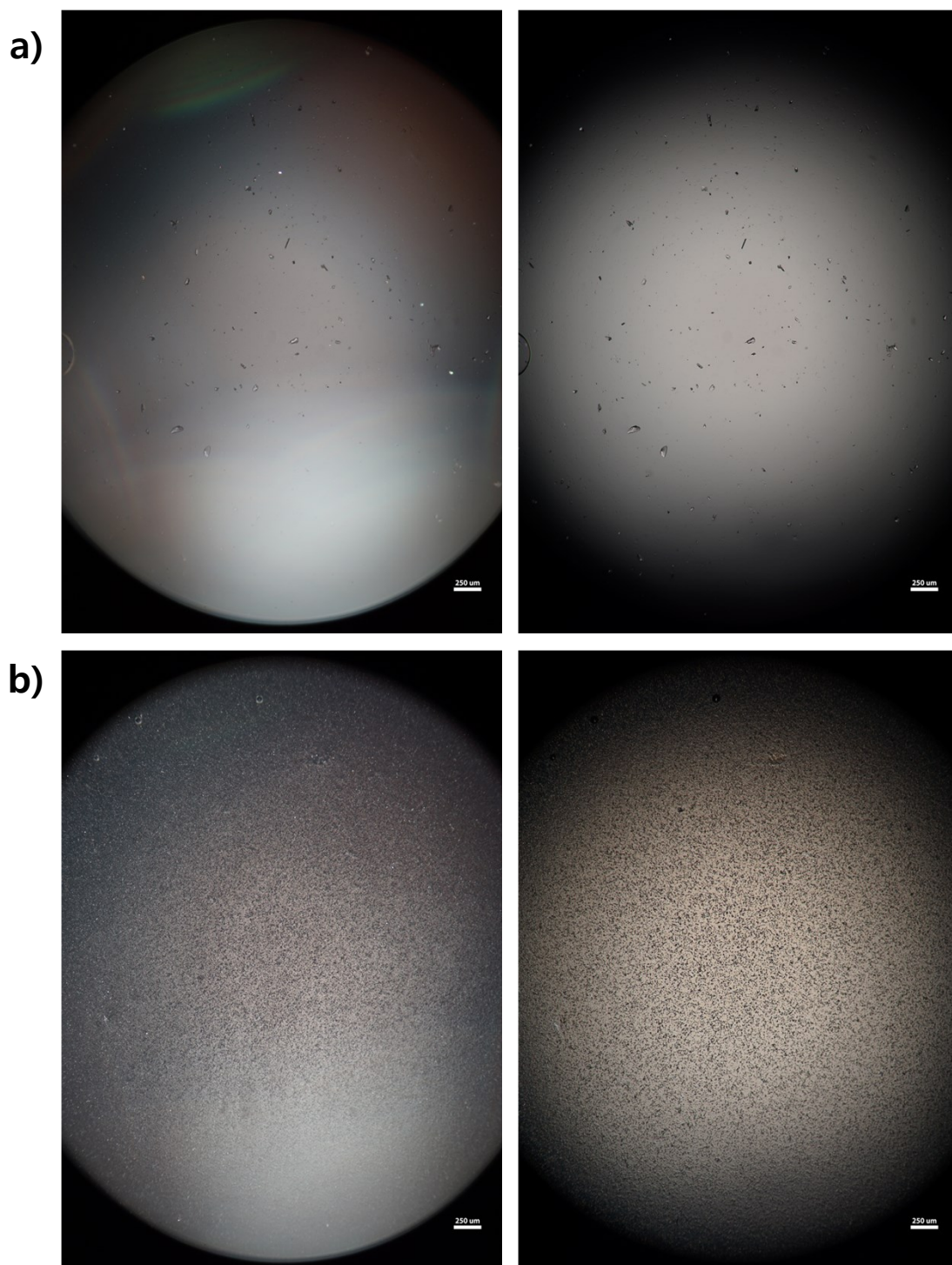
225 **3.1. Protein crystal populations**

226 Microscope images were acquired for each experiment using cross-polarized light (Fig. 3).
227 Particles of HEWL that appear white are birefringent and are very likely crystalline²⁷. Particles
228 that appear dark are amorphous precipitates of HEWL or crystals possessing a cubic (*i.e.*, isotropic)
229 lattice instead of the desired tetragonal structure. The inlet seed and outlet particles for
230 Experiments 1 to 3 are overwhelming anisotropic crystals (Fig. 3). Experiment 4, which is at
231 extremely high supersaturation σ_{max} , yielded minimal anisotropic crystals (Fig. 4). The production
232 of different solid states during particle formation operating under different magnitude
233 supersaturation is commonly observed for small molecule²⁸, and can certainly occur for protein
234 molecules which have many more degrees of freedom.



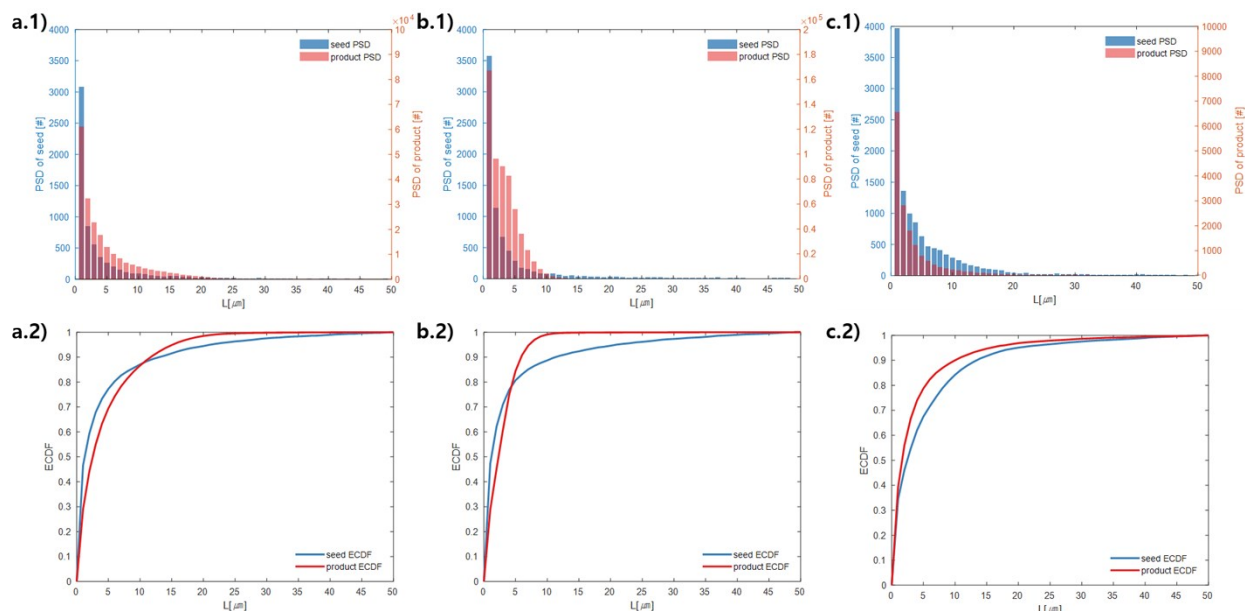
235

236 Figure 3. Representative micrographs from HEWL DoE Experiments 1–3. The upper image in each set is
 237 representative of the seed PSD used in the associated experiment. The lower image in each set is
 238 representative of the outlet PSD generated by the associated experiment. All images were acquired under
 239 cross-polarized lighting conditions using identical microscope aperture, condenser, and magnification
 240 (40X) settings. The scale bars are 250 μm in all images. (a.1) Seed of Experiment 1. (a.2) Outlet of
 241 Experiment 1. (b.1) Seed of Experiment 2. (b.2) Outlet of Experiment 2. (c.1) Seed of Experiment 3. (c.2)
 242 Outlet of Experiment 3.



243
 244 Figure 4. Representative micrographs from Experiment 4. The left image in each set was acquired under
 245 cross-polarized lighting conditions, while the right image was captured using plane polarized light. The
 246 crystal sample as not repositioned between image acquisitions. Identical microscope aperture, condenser,
 247 and magnification (40X) settings were used for all four images. The scale bars are 250 μm in all images.
 248 (a) Seed. (b) Outlet.

249



250

251 Figure 5. Measured particle size distribution (upper) and cumulative distribution function (lower) of seed
252 (blue) and product (orange) crystals. (a.1) and (a.2), (b.1) and (b.2), and (c.1) and (c.2) are for Experiments
253 1, 2, and 3 (summation of replicates), respectively. For all images, the horizontal axes are crystal length
254 (μm). The vertical axes are different for the seed and product crystals. As stated in Section 2.3, only particles
255 that exhibited high-intensity constructive interference under cross-polarized light (Fig. 3) were considered
256 crystals to calculate these PSDs.

257

258 With the image analysis procedure described in Section 2.3, micrographs of Experiments 1, 2,
259 and 3 were used to measure the PSDs of the seed and generated crystals in Fig. 5 (Experiment 4
260 was excluded from the analysis since the particles have a different solid state and so would have
261 different solubility and crystallization kinetics). The crystallization conditions in Experiments 1
262 and 2 yielded markedly different final PSDs than for Experiment 3. The leftward shift of the
263 experimental cumulative distribution functions (ECDFs) for Experiments 1 and 2 from relatively
264 heavy-tailed seed populations to substantially more monodisperse final distributions of small
265 crystals ($L < 30 \mu\text{m}$) suggests that, at an initial $\sigma_{max} \geq 5$, nucleation of HEWL crystals was strongly
266 favored over the growth of existing particles. In contrast, the product PSD is much more similar

266 to the seed PSD in Experiment 3, with a similar level of broadness. The resulting PSDs are
 267 consistent with the temperatures used in the experiments (Table 1). The temperature in Experiment
 268 1 was dropped to its lowest value at the crystallizer inlet and kept the value low, which would
 269 promote nucleation, until increasing the temperature at the end to promote growth. The large
 270 number of nuclei generated upstream in Experiment 1 would limit the size in which the crystals
 271 can grow downstream. The temperature in Experiment 2 also dropped to a low value at the
 272 crystallizer inlet, then was raised which would result in dissolution, and then the temperature was
 273 dropped to a very low value, and then kept low until the outlet. The large number of nuclei
 274 generated upstream would then largely be dissolved in the dissolution part of the crystallizer, but
 275 then a burst of nuclei would be generated again, which would then grow. The temperature in
 276 Experiment 3 was monotonically decreased by small reductions (Table 1), which resulted in much
 277 less nuclei formulation. Taken collectively, Fig. 5 demonstrates that, even over residence times as
 278 short as 25–30 minutes, the continuous protein crystallization system can be used to tune the
 279 characteristics of the protein crystal populations.

280 Table 2. Summary statistics for seed and product populations used in Experiments 1–3. N_T is the total
 281 number of crystals, $\bar{L}_{1,0}$, $\bar{L}_{2,0}$, and $\bar{L}_{3,0}$ are the mean crystal length (μm), surface area (μm^2), and volume
 282 (μm^3) in given experiments (summation of replicates), respectively. All mean size statistics were calculated
 283 using moments of the analytical derivatives of the ECDFs reported in Fig. 5. All N_T values were determined
 284 directly from the PSDs reported in these same figures.

Moment	Experiment 1		Experiment 2		Experiment 3	
	Seed	Product	Seed	Product	Seed	Product
N_T	6.7×10^3	2.1×10^5	7.6×10^3	5.8×10^5	1.2×10^4	1.7×10^4
$\bar{L}_{1,0}$	5.7	5.0	5.4	3.3	6.8	4.9
$\bar{L}_{2,0}$	1.3×10^2	5.5×10^1	1.3×10^2	1.9×10^1	1.6×10^2	9.3×10^1
$\bar{L}_{3,0}$	5.7×10^3	1.1×10^3	5.4×10^3	3.1×10^2	7.4×10^3	3.9×10^3

285 Continuously differentiable analytical expressions for these ECDFs were fitted using
286 piecewise cubic Hermite interpolating polynomials and used to calculate the summary statistics in
287 Table 2 via

$$f(L) = \frac{n(L)}{N_T}, \quad (1)$$

$$\bar{L}_{p,0} = \int_0^{\infty} L^p f(L) dL, p = 1, 2, \dots \quad (2)$$

288 where $f(L)$ is the number normalized PSD and $\bar{L}_{p,0}$ are weighted mean crystal sizes²⁹.

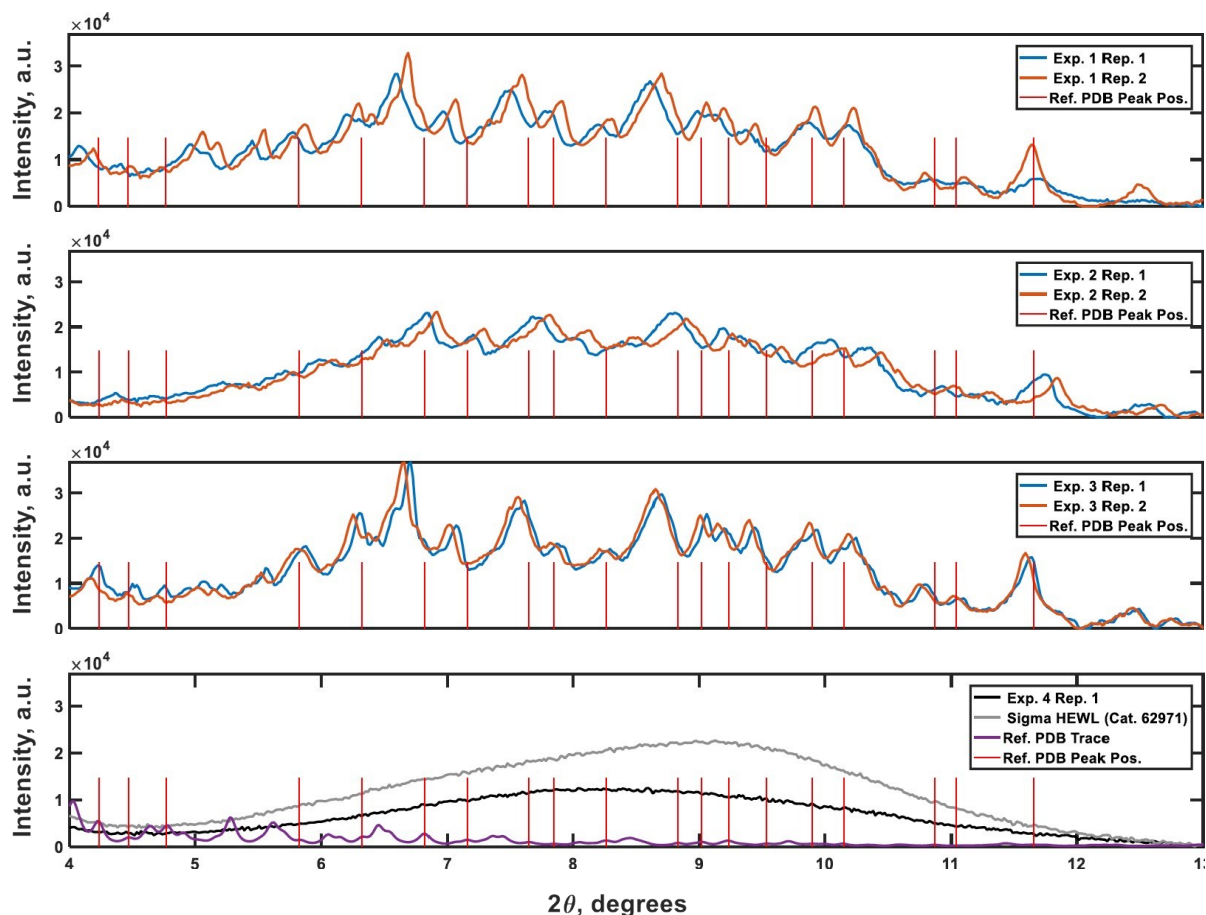
289 The above observations from Fig. 5 are seen in the summary statistics in Table 2. Given that
290 all PSDs were acquired from consistent total volumes of well-mixed slurries, the fact that

291 $\frac{N_{T,product}}{N_{T,seed}} > 10$ for Experiments 1 and 2 and ~ 1 for Experiment 3 indicates that Experiments 1 and
292 2 produced a much larger number of small crystals than Experiment 3. Further, for Experiments 1
293 and 2, nucleation was so strongly favored the process resulted in a drastic decrease in the mean
294 crystal volume $\bar{L}_{3,0}$ ($< 0.2x$) between the inlet and outlet of the system.

295 **3.2. Structural characterization of HEWL**

296 PXRD was employed as an orthogonal method to assess the qualitative crystallinity of all
297 samples generated and confirm the results of cross-polarized microscopy. Fig. 6 plots low angle
298 diffractograms for each of Experiments 1–4 from top to bottom. Where appropriate, diffractograms
299 for replicate experiments are plotted on common axes. Additionally, an idealized powder
300 diffractogram (bottom panel; purple line) for tetragonal HEWL served as a reference. All samples
301 collected at the outlet of the crystallizer during Experiments 1–3 exhibit relatively defined
302 diffraction peaks that match reference peak positions to within $\pm 0.5^\circ 2\theta$, suggesting that a

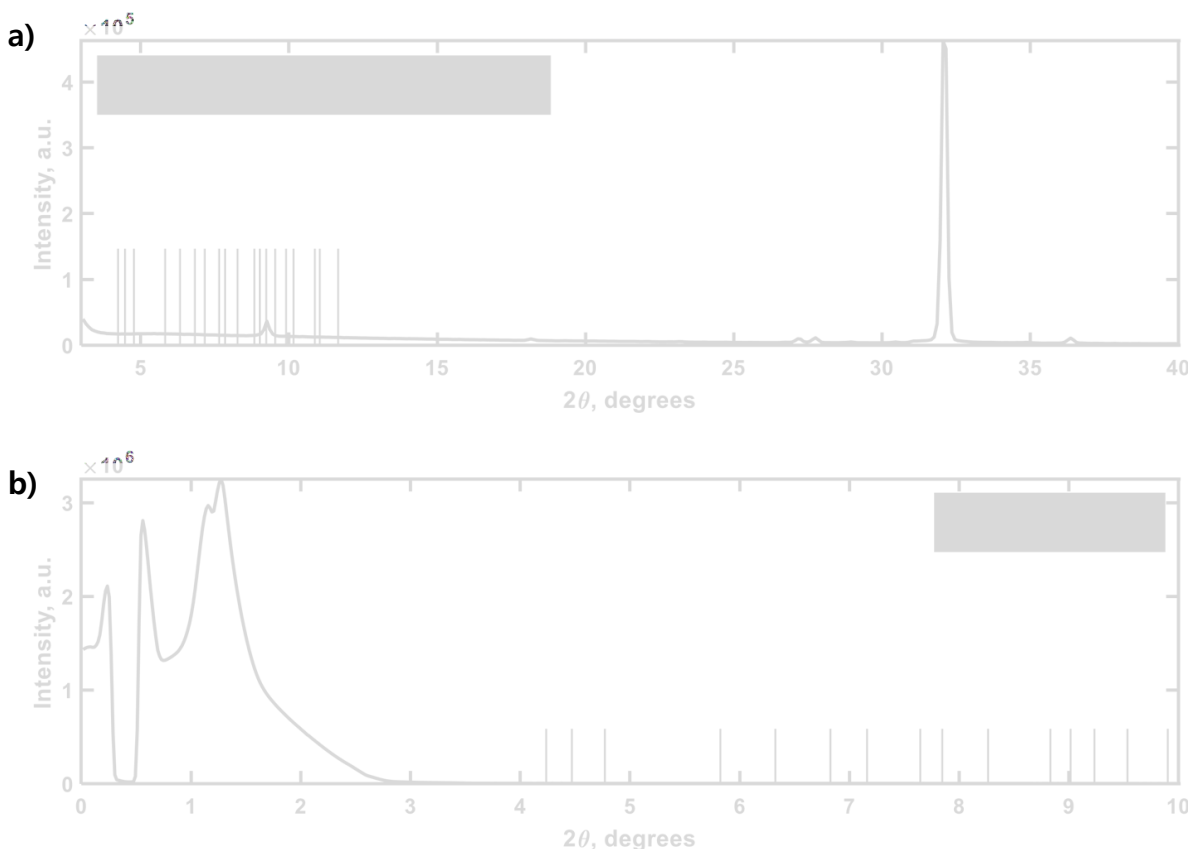
303 substantial fraction of the particles formed in each run was crystalline tetragonal HEWL. This
304 small offset in 2θ can likely be attributed to the higher resolution and signal-to-noise ratio of single-
305 crystal to powder XRD³⁰. Differences in the number of structure-bound water molecules between
306 samples could also convolute the traces. The systematic translation in 2θ evident between each
307 pair of traces for Experiments 1–3 is the result of small ($O(mm)$) differences in the positioning of
308 each sample within the focusing circle of the diffractometer³¹. While the PXRD data unequivocally
309 corroborate the formation of crystals in Experiments 1–3, all six diffractograms exhibit a broad
310 parabolic baseline (‘halo’) that indicates the presence of some amorphous or short-range ordered
311 nanocrystalline phases of matter³². Although techniques for estimating the relative ratio of
312 amorphous to crystalline material in PXRD traces exist (*e.g.*, the Rietveld method), they are
313 generally regarded as being difficult to implement and subject to large uncertainties³³. A
314 comparison of the top three panels of Fig. 6 to the black trace (Exp. 4; confirmed amorphous
315 precipitate) in the bottom panel of the figure, however, bolsters the claim that Experiments 1–3
316 yielded HEWL particles exhibiting significant crystalline character. HEWL analyzed as received
317 from the manufacturer also produced a purely amorphous diffractogram (Fig. 6; bottom panel;
318 gray line), which confirms the ability of the end-to-end seed population preparation and
319 crystallization process to generate long-range ordered protein particles from otherwise disordered
320 precursor materials.



321
 322 Figure 6. Powder X-ray diffraction traces characterizing the crystallinity of samples generated during the
 323 experiments. Plots 1–3 (top to bottom) are the PXRD traces gathered for material generated in Experiments
 324 1–3, respectively. The 4th plot shows reference non-crystalline spectra for manufacturer-supplied HEWL,
 325 and HEWL intentionally precipitated out of solution using the CCHEx platform (black; Exp. 4). The purple
 326 trace in the bottommost plot is an idealized PXRD diffractogram calculated using publicly available single-
 327 crystal XRD data banked in the RCSB Protein Data Bank (ID: 3wun). The vertical red lines in each plot
 328 correspond to the positions of a subset of the critical peaks in the idealized PXRD trace. The intensity of
 329 the lines is arbitrary.

330 Lastly, negative control diffractograms for a blank sample tray and vacuum-dried HEWL
 331 dissolution buffer are presented in Fig. 7. The diffractogram for the blank sample tray exhibits a
 332 flat baseline for $2\theta \geq 3^\circ$. Similarly, the HEWL dissolution buffer diffractogram exhibits only a
 333 single peak within the range $9.5^\circ \leq 2\theta \leq 10^\circ$, which is characteristic of NaOAc. These controls

334 indicate that neither the dissolution buffer nor the sample tray are expected to obscure the PXRD
335 peaks of HEWL under the measurement conditions employed³⁴.



336
337 Figure 7. Control PXRD diffractograms of HEWL dissolution buffer (a) and zero-background sample tray
338 (b). The vertical red lines in each panel correspond to a subset of the critical peak positions in an idealized
339 diffractogram calculated from single-crystal XRD data for tetragonal HEWL (PDBid: 3wun). (a) The
340 doublet at $\sim 27.5^\circ 2\theta$ are characteristic of NaCl. The low intensity peak at $\sim 9^\circ 2\theta$ is characteristic of NaOAc
341 (and is subject to shift above $10^\circ 2\theta$ due to variations in molecular hydration). (b) The high-intensity
342 baseline below $3^\circ 2\theta$ is likely the result of direct beam scattering off of the sample tray itself at these
343 extremely shallow angles.

344

345 **4. Conclusion**

346 A continuous slug-flow crystallizer comprising reconfigurable, feedback-controlled, counter-
347 current heat exchangers is applicable to mediating protein crystallization. Experiments using hen

348 egg white lysozyme as the model protein showed that particle size distributions could be
349 reproducibly manipulated using temperature gradients alone over a residence time of only 25–30
350 minutes. The formation of XRD-crystalline particles of HEWL was robust to maximum relative
351 supersaturation gradients spanning two orders of magnitude, with σ_{max} values ≥ 5 favoring the
352 nucleation over the growth of existing crystals. In addition, the in-line mixing of concentrated
353 precipitant solution allowed σ_{max} values as large as 220 to be achieved in concert with steep
354 temperature gradients. Powder x-ray diffraction indicated that σ_{max} of this magnitude
355 overwhelmingly favored the formation of amorphous precipitates, which would have lower
356 stability and higher solubility than crystals. The low cost and disposable nature of the slug-flow
357 continuous crystallizer (~\$100 for the disposable tubing) and the ability to tune the particle size
358 distribution suggest that this crystallization platform could be suitable in applications where the
359 protein therapeutic is delivered in crystalline form, since the PSD directly affects the rate in which
360 the protein would be absorbed by the body.

361 **Conflict of Interest**

362 There are no conflicts to declare.

363 **Acknowledgement**

364 This study was supported by the Bill & Melinda Gates Foundation [OPP1154682]. The
365 findings and conclusions contained within are those of the authors and do not necessarily reflect
366 positions or policies of the Bill & Melinda Gates Foundation. Financial support is acknowledged
367 from the Engineering Development Research Center (EDRC) at Seoul National University for
368 Yongkyu Lee. Leia Dwyer and Carlos Sieperman are acknowledged for PXRD training.

- 370 1. Gagnon, P., Technology trends in antibody purification. *Journal of Chromatography A*
371 **2012**, *1221*, 57-70.
- 372 2. Jungbauer, A., Continuous downstream processing of biopharmaceuticals. *Trends in*
373 *Biotechnology* **2013**, *31* (8), 479-492.
- 374 3. Konstantinov, K. B.; Cooney, C. L., White paper on continuous bioprocessing May 20–21
375 2014 continuous manufacturing symposium. *Journal of Pharmaceutical Sciences* **2015**, *104* (3),
376 813-820.
- 377 4. Kelley, B., Very large scale monoclonal antibody purification: The case for conventional
378 unit operations. *Biotechnology Progress* **2008**, *23* (5), 995-1008.
- 379 5. Kelley, B., Industrialization of mAb production technology: The bioprocessing industry at
380 a crossroads. *mAbs* **2009**, *1* (5), 443-452.
- 381 6. Hong, M. S.; Severson, K. A.; Jiang, M.; Lu, A. E.; Love, J. C.; Braatz, R. D., Challenges
382 and opportunities in biopharmaceutical manufacturing control. *Computers & Chemical*
383 *Engineering* **2018**, *110*, 106-114.
- 384 7. Zydney, A. L., Continuous downstream processing for high value biological products: A
385 Review. *Biotechnology and Bioengineering* **2015**, *113* (3), 465-475.
- 386 8. Bryntesson, M.; Hall, M.; Lacki, K. Chromatography method. U.S. Patent 7,901,581, Mar
387 8, 2011.
- 388 9. Warikoo, V.; Godawat, R.; Brower, K.; Jain, S.; Cummings, D.; Simons, E.; Johnson, T.;
389 Walther, J.; Yu, M.; Wright, B.; McLarty, J.; Karey, K. P.; Hwang, C.; Zhou, W.; Riske, F.;
390 Konstantinov, K., Integrated continuous production of recombinant therapeutic proteins.
391 *Biotechnology and Bioengineering* **2012**, *109* (12), 3018-3029.
- 392 10. Eggersgluess, J.; Wellsandt, T.; Strube, J., Integration of aqueous two-phase extraction
393 into downstream processing. *Chemical Engineering & Technology* **2014**, *37* (10), 1686-1696.
- 394 11. Hammerschmidt, N.; Tscheliessnig, A.; Sommer, R.; Helk, B.; Jungbauer, A., Economics
395 of recombinant antibody production processes at various scales: Industry-standard compared to
396 continuous precipitation. *Biotechnology Journal* **2014**, *9* (6), 766-775.
- 397 12. Neugebauer, P.; Khinast, J. G., Continuous crystallization of proteins in a tubular plug-
398 flow crystallizer. *Crystal Growth & Design* **2015**, *15* (3), 1089-1095.
- 399 13. Crowell, L. E.; Lu, A. E.; Love, K. R.; Stockdale, A.; Timmick, S. M.; Wu, D.; Wang, Y.;
400 Doherty, W.; Bonnyman, A.; Vecchiarello, N.; Goodwine, C.; Bradbury, L.; Brady, J. R.; Clark,
401 J. J.; Colant, N. A.; Cvetkovic, A.; Dalvie, N. C.; Liu, D.; Liu, Y.; Mascarenhas, C. A.; Matthews,
402 C. B.; Mozdierz, N. J.; Shah, K. A.; Wu, S.-L.; Hancock, W. S.; Braatz, R. D.; Cramer, S. M.;
403 Love, J. C., On-demand manufacturing of clinical-quality biopharmaceuticals. *Nature*
404 *Biotechnology* **2018**, *36* (10), 988-995.
- 405 14. Lu, A. E.; Paulson, J. A.; Mozdierz, N. J.; Stockdale, A.; Versypt, A. N. F.; Love, K. R.;
406 Love, J. C.; Braatz, R. D., Control systems technology in the advanced manufacturing of biologic
407 drugs. In *Proc. of the IEEE Conference on Control Applications*, 2015; pp. 1505-1515.
- 408 15. Hekmat, D., Large-scale crystallization of proteins for purification and formulation.
409 *Bioprocess and Biosystems Engineering* **2015**, *38* (7), 1209-1231.
- 410 16. McPherson, A., Introduction to protein crystallization. *Methods* **2004**, *34* (3), 254-265.

- 411 17. Russo Krauss, I.; Merlino, A.; Vergara, A.; Sica, F., An overview of biological
412 macromolecule crystallization. *International Journal of Molecular Sciences* **2013**, *14* (6), 11643-
413 11691.
- 414 18. Baker, J. C.; Roberts, B. M. Preparation of stable insulin analog crystals. U.S. Patent
415 5,597,893, Jan 28, 1997.
- 416 19. Mitragotri, S.; Burke, P. A.; Langer, R., Overcoming the challenges in administering
417 biopharmaceuticals: formulation and delivery strategies. *Nature Reviews Drug Discovery* **2014**,
418 *13* (9), 655-672.
- 419 20. Zhang, D.; Xu, S.; Du, S.; Wang, J.; Gong, J., Progress of pharmaceutical continuous
420 crystallization. *Engineering* **2017**, *3* (3), 354-364.
- 421 21. Mozdierz, N. J. Developing scalable and modular technologies for continuous
422 biopharmaceutical production. Ph.D. thesis. Massachusetts Institute of Technology, Cambridge,
423 MA, 2018.
- 424 22. Mozdierz, N. J.; Lee, Y.; Hong, M. S.; Benisch, M. H. P.; Rasche, M. L.; Tropp, U. E.;
425 Jiang, M.; Myerson, A. S.; Braatz, R. D., Mathematical modeling and experimental validation of
426 continuous slug-flow tubular crystallization with ultrasonication-induced nucleation and spatially
427 varying temperature. *Chemical Engineering Research and Design* **2021**, *169*, 275-287.
- 428 23. Pirkle, J. C.; Rasche, M. L.; Braatz, R. D.; Jiang, M., CHAPTER 5 Slug-flow continuous
429 crystallization: Fundamentals and process intensification. In *The Handbook of Continuous*
430 *Crystallization*, The Royal Society of Chemistry: Croydon, UK, 2020; pp. 219-247.
- 431 24. Forsythe, E. L.; Judge, R. A.; Pusey, M. L., Tetragonal chicken egg white lysozyme
432 solubility in sodium chloride solutions. *Journal of Chemical & Engineering Data* **1999**, *44* (3),
433 637-640.
- 434 25. Chayen, N. E., Methods for separating nucleation and growth in protein crystallisation.
435 *Progress in Biophysics and Molecular Biology* **2005**, *88* (3), 329-337.
- 436 26. Pons Siepermann, C. A.; Huang, S.; Myerson, A. S., Nucleation inhibition of benzoic acid
437 through solution complexation. *Crystal Growth & Design* **2017**, *17* (5), 2646-2653.
- 438 27. Dombrowski, R. T., 1 - Microscopy techniques for analyzing the phase nature and
439 morphology of biomaterials. In *Characterization of Biomaterials*, Jaffe, M.; Hammond, W.;
440 Toliás, P.; Arinze, T., Eds. Woodhead Publishing: Waltham, MA, 2013; pp. 1-33.
- 441 28. Myerson, A., *Handbook of Industrial Crystallization*. Butterworth-Heinemann: Woburn,
442 MA, 2002.
- 443 29. Ranodolph, A., *Theory of Particulate Processes: Analysis and Techniques of Continuous*
444 *Crystallization*. Elsevier: New York, 2012.
- 445 30. Varlashkin, P., Approaches to quantification of amorphous content in crystalline drug
446 substance by powder X-ray diffraction. *American Pharmaceutical Review* **2011**, *14* (1), 22-28.
- 447 31. Speakman, S., Basics of X-Ray Powder Diffraction: Training to Become an Independent
448 User of the X-Ray SEF at the Center for Materials Science and Engineering at MIT. *Online*][Cited:
449 April 6, 2017.] [http://prism.mit.edu/xray/oldsite/Basics%20of%20X-Ray%20Powder%](http://prism.mit.edu/xray/oldsite/Basics%20of%20X-Ray%20Powder%20Diffraction.pdf)
450 [20Diffraction.pdf](http://prism.mit.edu/xray/oldsite/Basics%20of%20X-Ray%20Powder%20Diffraction.pdf).
- 451 32. Bates, S.; Zografí, G.; Engers, D.; Morris, K.; Crowley, K.; Newman, A., Analysis of
452 amorphous and nanocrystalline solids from their X-ray diffraction patterns. *Pharmaceutical*
453 *Research* **2006**, *23* (10), 2333-2349.

- 454 33. Kemethmüller, S.; Roosen, A.; Goetz-Neunhoeffler, F.; Neubauer, J., Quantitative analysis
455 of crystalline and amorphous phases in glass–ceramic composites like LTCC by the Rietveld
456 method. *Journal of the American Ceramic Society* **2006**, 89 (8), 2632-2637.
- 457 34. Kumar, R.; Vyas, S.; Kumar, R.; Dixit, A., Development of sodium acetate trihydrate-
458 ethylene glycol composite phase change materials with enhanced thermophysical properties for
459 thermal comfort and therapeutic applications. *Scientific Reports* **2017**, 7 (1), 1-11.

460